MnO 2 -MXene Composite as Electrode for Supercapacitor

Yachao Zhu, Khalil Rajouâ, Steven Le Vot, Olivier Fontaine, Patrice Simon, Frédéric Favier

MnO_2-MXene composite as electrode for supercapacitor

Yachao Zhu,[1,2,3] Khalil Rajouâ,[1,3] Steven Le Vot,[1,3] Olivier Fontaine,[4,5] Patrice Simon,[2,3] and Frédéric Favier[1,3]

1. Institut Charles Gerhardt Montpellier (ICGM), Univ. Montpellier, CNRS, ENSCM, Montpellier, France

2. CIRIMAT, Université de Toulouse, CNRS, INPT, Université Paul Sabatier, 118 route de Narbonne, 31062, Toulouse, France

3. Réseau sur le Stockage Electrochimique de l'énergie (RS2E), FR CNRS 3459, France

4. School of Energy Science and Engineering, Vidyasirimedhi Institute of Science and Technology (VISTEC), Rayong, 21210, Thailand

5. Institut Universitaire de France, 75005 Paris, France

email : frederic.favier@umontpellier.fr

KEYWORDS: MnO_2, MXene, capacitance, electrolyte, energy

ABSTRACT: A MnO_2-MXene composite material is reported, in which MnO_2 particles have been grown onto Ti_3C_2 MXene flakes. Thanks to its interconnected structure, it can not only boost the low electrical conductivity of MnO_2, but also suppress the restacking of MXene flakes. As an electrode material in a three-electrode cell, the composite showed greater capacitance and improved stability performance than raw MnO_2 in both KOH and Na_2SO_4 aqueous electrolytes. Equipped with MnO_2–MXene composite material as positive and activated carbon as negative, an asymmetric device using Na_2SO_4 as electrolyte displayed an energy density of 20 Wh kg^{-1} at 500 W kg^{-1} power density. On the other hand, the device operated in KOH electrolyte showed an energy density of 17 Wh kg^{-1} at 400 W kg^{-1}, and 11 Wh kg^{-1} at 8 kW kg^{-1}.

INTRODUCTION

Supercapacitors (SCs)[1], including electrochemical double-layer capacitors (EDLCs)[2] and redox-based pseudocapacitors[3], have been extensively studied as promising and efficient candidates for energy storage systems thanks to many attractive features that advantageously supplement those of batteries[4]. These include high power density, fast charge-discharge rate and long cycle life[5,6]. In contrast, their energy density is lower. Carbon-based EDLCs[7] usually show a high rate capability thanks to their electrostatic charge storage mechanism based on the reversible adsorption-desorption of electrolytic ions onto the large surface area of the electrode material during quick charge-discharge processes[8]. Various materials such as porous carbons[9-14] and graphene[15-17] have been explored as

electrode materials and the vast majority of the supercapacitors commercialized worldwide are activated carbon -based EDLC devices. On the other hand, oxide-based pseudocapacitive materials[18] store charges through fast and reversible redox reactions near the surface of the material, leading to attractive capacitances[19,20]. In comparison with EDLCs, energy density is greater thanks to the Faradaic contribution but because of the kinetics of the involved redox reactions (intrinsically slower than electrosorption), power is less attractive. Many metal oxides such as RuO_2[21-24] and MnO_2[25-27] have been confirmed as suitable pseudocapacitive electrode materials. The impact on the storage performance of both electronic and crystallographic structures of the oxides has been demonstrated.[28-32] As an example, storage performance, including rate capabilities, has been demonstrated to depend on the structure of the pseudocapacitive oxide. This is especially true with MnO_2 polymorphs built on 1 to 3D structures, either on channeled, layered or compact arrangements allowing the more or less efficient solid-state diffusion of compensating cations involved in the charge storage mechanism.[35-38] On the other hand, the poor intrinsic electronic conductivity of MnO_2 limits its overall rate capability, which inhibits the electrode capacitance to reach the theoretical value at ~1380 F/g.[33,34] As such, improving the electronic conductivity of MnO_2-based electrode materials remains a consistent strategy to reach greater performance, especially rate capability, and, consequently, greater device power.

Recently, two-dimensional transition metal nitrides/carbides (MXenes)[39,40] have been successfully prepared by etching of A layers from MAX phases, giving a few atoms thick layered extended family with a general formula $Mn_{+1}X_nT_x$, where M represents a transition metal, X is C and/or N, and T_x stands for surface terminations[41-43]. Thanks to their high accessible surface areas promoted by a 2D structure as well as the high electrical conductivity of the carbide-core layer (~4,000 $S.cm^{-1}$), MXene materials can achieve attractive electrochemical performance in aqueous electrolytes, with capacitances beyond 250 F g^{-1} or 1,500 $F.cm^{-3}$ [44-50].

Back in 2016, Rakhi et al has reported on the synthesis and electrochemical characterization of MnO_2 nanowhiskers on MXene surfaces[51]. This is the ε form of MnO_2, also known as MnO_2 Ramsdelite, which was actually precipitated at the surface of exfoliated flakes of Ti_3C_2. The Ramsdelite structure is built on edge-sharing MnO_6 octaedra in a 1x2 configuration forming channels in which alkali cations are stabilizing the structural arrangement, Therefore, its 1D structure provides ε-MnO_2 with a fair ionic conductivity and, consequently, a pseudocapacitive behavior in neutral aqueous electrolytes with fair charge storage capabilities when used as electrode material in a supercapacitor[52]. As such, these authors claimed up to 212 F g^{-1} capacitance (at 1 A g^{-1} current density) could be obtained with an electrode based on the prepared ε-MnO_2/Ti_3C_2 composite cycled in a 30wt% KOH electrolyte. Despite this attractive performance and the elegance of the synthetic approach, there is still room for improvement. This, especially by considering more performing MnO_2 polymorphs to decorate the Ti_3C_2 MXene flakes. This could be MnO_2 birnessite, or δ-MnO_2, which has shown, thanks to its more open 2D layered structure, up to twice the capacitance, as electrode material, than that of Ramsdelite[52]. Rakhi et al choose to use a symmetric two electrode setup while an asymmetric device with an activated carbon negative electrode, for example, would have been more realistic to discuss power and energy densities. Moreover, they limited their study to a single KOH based electrolyte while MnO_2, as a pseudocapacitive electrode material, is known to show enhanced electrochemical performance when operated in safer neutral sulfate or nitrate -based aqueous electrolytes.[53,54,55,56] Data in Table S1 and associated references are supporting these observations. With the objective to select a more performing MnO_2 material to be incorporated in a nanocomposite with Ti_3C_2 MXene, we initially studied changes in the crystalline structure of MnO_2 and associated electrochemical performance, correlated with the preparation temperature. Interestingly, when increasing the temperature, a material based on layers (δ-MnO_2) together with fibers (α-MnO_2) was obtained, showing an attractive cooperative electrochemical behavior taking advantage of the greater capacitance from the δ phase and greater rate capability from the α phase. Furthermore, exfoliated MXene was used to prepare a composite material in which MnO_2 particles were grown, at the selected temperature, on MXene flakes providing an improved conductivity and preventing the restacking of MXenes layers. Thanks to these advanced features, the MnO_2eMXene (MeM) composite electrode was first evaluated in terms of specific capacitance, rate and cycling capabilities either in KOH and Na_2SO_4 electrolytes. The composite and activated carbon were used

as positive and negative electrode, respectively, to fabricate an asymmetric device. Thanks to the large potential window of 2V in Na_2SO_4, AC//MeM-Na device showed attractive energy and power densities. In KOH electrolyte, AC//MeM-K device showed slightly lower but fair energy and power performance.

MATERIALS AND METHODS

Preparation of Ti_3C_2 MXene suspension and film

1 g of LiF and 20 mL of 9 M HCl were mixed and stirred in a plastic bottle. After a few minutes, 1 g Ti_3AlC_2 grey powder was progressively added to the mixture. This etching process was kept at 35 ^oC for 24h under constant stirring. Accordingly, Ti_3C_2 MXene flakes were repeatably rinsed off by ultrapure water to rise the pH of the effluent up to about 6. After re-dispersing MXene flakes in 250 mL pure water, the flakes were exfoliated by sonication for one hour. The un-exfoliated Ti_3C_2 material was removed by centrifugation for 1 h. Finally, a Ti_3C_2 MXene suspension was obtained. The MXene film was prepared by an easy one-step method. In more details, a given mass of MXene suspension in water was slowly filtered on a PTFE membrane under vacuum. The resulting Ti_3C_2 MXene film was dried in a glass tube under vacuum before use.

Preparation of MnO_2 by co-precipitation

0.1272 g $MnCl_2$ and 0.24 g $KMnO_4$ were respectively dispersed in ultra-pure 20 mL H_2O under constant stirring. Then, the $KMnO_4$ solution was added drop by drop to the $MnCl_2$ solution (5 minutes duration operation). The resulting suspension was transferred in a laboratory reflux apparatus and heated at a 120 ^oC setpoint temperature for 6 h. After filtration, collected brown MnO_2 powders were dried at 80 ^oC in air. Additionally, the effect of the co-precipitation temperature was investigated and syntheses were conducted at 30, 80, 140 °C setpoint temperatures. Corresponding samples are referred as M-30, M-80, M-120 and M-140 depending on the temperature the powder was prepared.

Preparation of MnO_2eMXene

20 mL of a mixture with 20.0 mg Ti_3C_2 MXene and 127.2 mg $MnCl_2$ was first prepared. Using the procedure as described above for the preparation of raw MnO_2, 20 mL $KMnO_4$ solution was slowly added and the resulting suspension was kept at a temperature of 120 °C, for 6 h. This synthesis temperature was chosen for reasons explained below. After drying, the MnO_2eMXene composite material was obtained.

XRD, SEM, TEM sampling and equipment

X-ray diffraction patterns of the prepared materials were obtained using a Phillips X'Pert diffractometer with Cu Kα radiation (λ=1.5405Å) in a Bragg-Brentano configuration. A JEOL JSM-6300F scanning electron microscope (SEM) was used to investigate the powder morphologies.

Sampling was done on dry powders on carbon tape. Energy-dispersive X-ray spectroscopy (EDX) and mapping in SEM was applied to analyze elemental compositions and distributions. Transmission electron microscopy (TEM) measurements were done using a JEOL 1200EX2 TEM instrument. Sampling was done on carbon-copper grids.

Electrochemical characterization

A VMP3 multi-channel Bio-Logic electrochemical workstation was used for all the electrochemical measurements done at controlled room temperature (23 °C) in a three-electrode configuration as well as in a Swagelok setup. Electrode discs were fabricated by first mixing the prepared materials (60%), acetylene black (30%) and PTFE (10%) in ethanol. The resulting paste was then rolled as a film, finally cut as 8 mm diameter round samples using a puncher tool. In the three-electrode setup, the working electrode was the synthesized materials, the reference electrodes were Hg/HgO (KOH) and Ag/AgCl (Na_2SO_4), and the counter electrode was a platinum foil. Gravimetric capacitances were normalized to the active material weight. The mass loadings of pure MnO_2 are given in Table S2. The weight loadings of composite are about 6.0 mg cm^{-2}. In the asymmetric device, a commercial activated carbon (PICA) was used as negative electrode. Electrode mass balancing was done by considering capacitances calculated from CVs done on individual electrodes in selected electrolytes.

RESULTS AND DISCUSSION

MnO_2 powders were prepared by a co-precipitation method using Mn^{2+} and MnO_4^{-1} as reductant and oxidant, respectively (Figure 1, top). Depending on the synthesis temperature (from 80 to 140 °C), resulting MnO_2 materials exhibited some discrepancies in their crystalline structure from δ to α phase, additionally following morphological changes from nano sheets to nano fibers. Furthermore, Ti_3C_2 MXene flakes were used as substrates to grow MnO_2 by the same co-precipitation method at a synthesis temperature of 120 °C, eventually resulting in a nanostructured MnO_2eMXene composite (Figure 1, bottom).

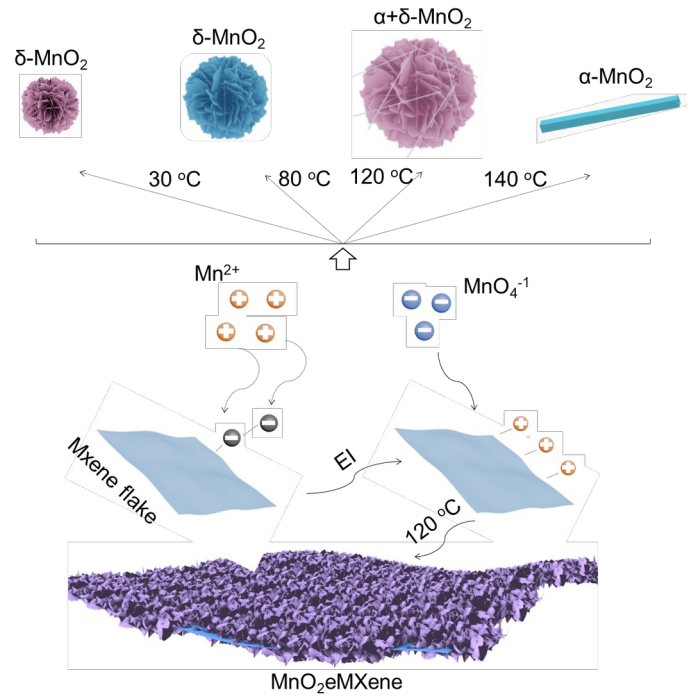

Figure 1. Schematic diagram of material preparations.

Structural changes in MnO_2 powders induced by the selected preparation temperature have been evidenced by XRD measurements (Fig. S1). For MnO_2-30 (black), MnO_2-80 (grey) and MnO_2-120 (blue) samples, corresponding to MnO_2 powders prepared at 30, 80 and 120 °C, respectively, diffraction peaks are indexed and correspond to δ-MnO_2 (Birnessite, JCPDS 1098[57,58]). This manganese dioxide morphotype shows a layered structure built on 2D layers of edge-sharing [MnO_6] octahedra. Whereas, a clear difference in the crystal structure is distinctly revealed in the XRD pattern of the MnO_2-140 sample, prepared at 140 °C. It exhibits a series of new peaks as well as the absence of the (001) peak previously at 66.28 °2θ. This pattern matches that of α-MnO_2 (Hollandite, JCPDS 44-0141) whose structure is built on 1D tunnels (2x2 edge-sharing MnO_6 octahedra). A closer look at the MnO_2-120 XRD pattern also shows some extra peaks of lower intensity, especially at 56.21 °2θ which corresponds to the (600) diffraction peak of the α-type structure. This latter suggests a mixture, mostly made of δ-MnO_2 and some α-MnO_2, to be obtained at 120 °C.

As the reaction temperature was increased, the powder morphologies evolved consistently with the structural changes pointed out by XRD analysis. The micro-morphology of prepared powders was studied by scanning electron microscopy measurements. In Fig. S2, the expected δ-MnO_2 “sand rose” morphologies are clearly observed in MnO_2-30 and MnO_2-80. These roughly spherical particles are made of disordered aggregated MnO_2 platelets. In contrast, at 140 °C, α-MnO_2 nano-rods and needles are mostly observed, together with a few “sand rose” particles. Finally, as suggested by XRD analysis, MnO_2-120 sample is confirmed as a mixture of both types of δ-MnO_2 and α-MnO_2 nano-crystals.

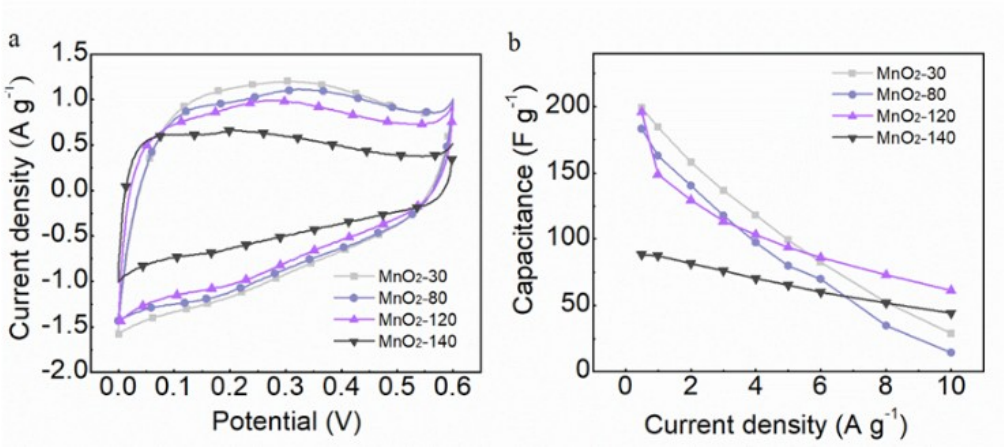

Figure 2. Electrochemical performances comparison of MnO_2 prepared at various reaction temperatures in 1 M KOH. (a) Cyclic voltammetry curves at 5 mV s^{-1} scan rate. (b) Comparison of specific capacitances from galvanostatic measurements at various current densities.

Electrodes based on the prepared MnO_2 materials were tested in a three-electrode setup in 1 M KOH electrolyte with the objective to evaluate the impact of their structure/morphology on their electrochemical behavior. Corresponding capacitances were calculated from cyclic voltammetry measurements at 5 mV s^{-1} scan rate from 0 to 0.6 V versus Hg/HgO reference electrode (Fig. 2a). Capacitances are detailed in Table S1 but a direct observation of the CV areas allows to compare the various electrode material performance: MnO_2-30 electrode CV displays the largest area in the series and correspondingly, the greatest capacitance at 181 F g^{-1}. As the synthesis temperature was increased, the capacitance of the resulting material decreased, and MnO_2-140 showed the lowest capacitance in the series at 98 F g^{-1}. This trend is assigned to the structural characteristics of the prepared MnO_2. δ-MnO_2 2D structure has been shown to be highly favorable to the diffusion in between MnO_2 layers of electrolytic cations involved in the charge storage mechanism. As such, corresponding capacitances are the greatest in the MnO_2-based electrode material family[52]. In contrast, α-MnO_2 built on more constraining 1D tunnels is less performing either in terms of ionic conductivity and capacitance.[62] Measured electrode capacitances are actually related to the δ-MnO_2/α-MnO_2 composition ratio. They decrease as the α-MnO_2 content increases while increasing the synthesis temperature. Capacitances were measured at various charge-discharge rates by galvanostatic measurements (Fig. 2b). Similarly, to CV measurements, it was found that, at a low current density such as 0.5 A g^{-1}, MnO_2-30 and MnO_2-80 electrode materials, mostly composed of δ-MnO_2, showed larger capacitances than α-MnO_2-rich material such as MnO_2-140. However, capacitances of MnO_2-30 and MnO_2-80 quickly decreased as the current density was increased. For example, the capacitance of MnO_2-30 -based electrode was 29 F g^{-1} and that of MnO_2-80 was 14 F g^{-1} at 10 A g^{-1}. The rate capabilities of these electrodes are as such, fairly limited. In contrast, while the capacitance of MnO_2-140 was limited to 88 F g^{-1} at 0.5 A g^{-1}, it was still 44 F g^{-1} at 10 A g^{-1}. Finally, not only could MnO_2-120 electrode deliver a high capacitance of 196 F g^{-1} at 0.5 A g^{-1}, but it also retained a 62 F g^{-1} capacitance at 10 A g^{-1}. This latter electrode behavior can be explained by

its specific composition based on a mixture of δ- and α-MnO_2. At low current density, δ-MnO_2 provides the electrode with its attractive low rate capacitance assigned to its 2D open structure and associated fair ionic conductivity, while α-MnO_2 component favorably contributes to the capacitance at high current density thanks to its greater electronic conductivity.[52] Thanks to this peculiar composition in the series, MnO_2-120 electrode material offers the best compromise in terms of rate capabilities, with enhanced capacitances in a wider range of charge-discharge regimes. Because of these well balanced electrochemical properties, 120 °C synthesis temperature was chosen for the preparation of MnO_2eMXene composite based on the precipitation of MnO_2 at the surface of exfoliated Ti_3C_2 MXene flakes.

X-ray diffraction (XRD) patterns of the prepared raw MnO_2-120 and MnO_2eMXene composite materials are depicted in Figure 3. As expected, MnO_2 powder prepared at 120 °C corresponds to the above described mixture made of δ-MnO_2 (mainly) and some α-MnO_2. The XRD pattern of the Ti_3C_2 MXene shows the usual features of restacked 2D materials with a series of diffraction peaks of decreasing intensity at greater diffraction angle. These correspond to the (002n) atomic layers of Ti_3C_2 MXene and are consistently measured at angles corresponding to the interlayer distance. The XRD pattern of the composite material obtained by precipitation of MnO_2 in presence of exfoliated Ti_3C_2 MXene layers at 120 °C retains the characteristics of the poorly crystallized MnO_2-120 material. Actually, only remain the main peaks from the pristine MnO_2. In contrast, the intense 002 peak of the MXene component almost completely vanishes. This is a proof that this synthetic method prevents exfoliated MXene layers to restack in the composite. This XRD analysis suggests that δ-MnO_2 actually grows at the surface of Ti_3C_2 MXene flakes made of a very few layers of Ti_3C_2. Moreover, a tendency of the MnO_2 layers to grow parallel to those of MXene is supported by the greater intensity of the (111) peak, characteristic of a preferential orientation of the MnO_2 layers in the composite.

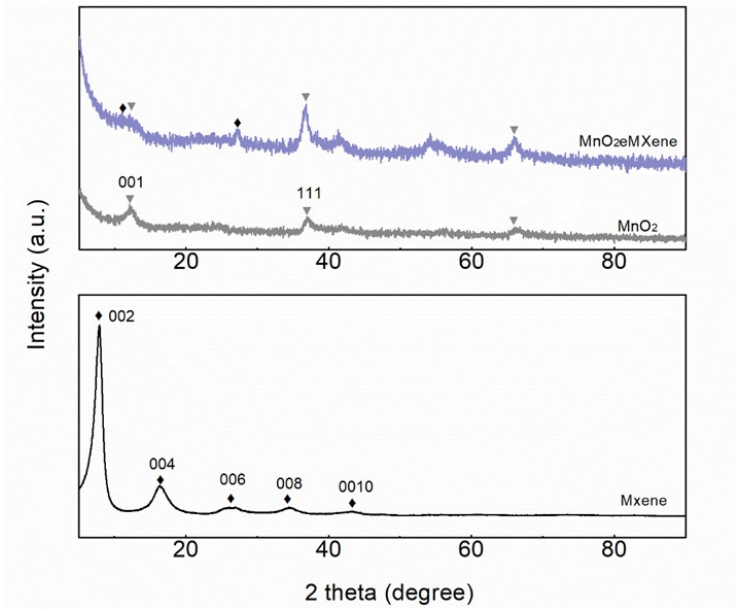

Figure 3. XRD patterns of MXene, δ-MnO_2 and MnO_2eMXene composite.

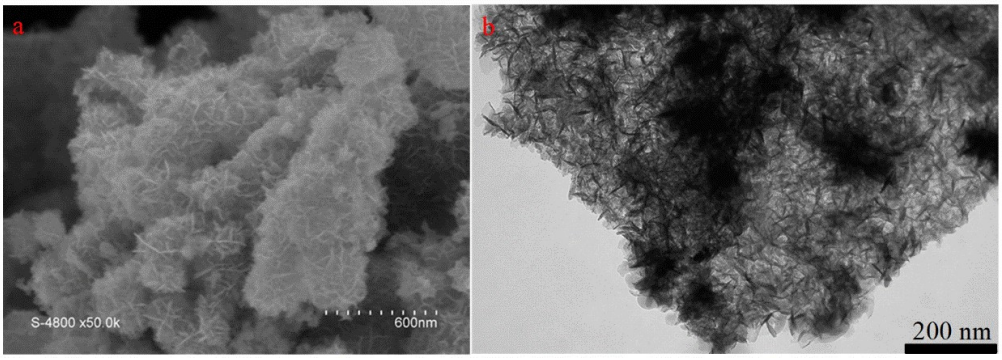

Figure 4. SEM and TEM images of MnO_2eMXene composite.

When MXene flakes are introduced as substrates in the synthetic medium, Mn^{2+} cations are first adsorbed on negatively charged MXene layers[59-61] by electrostatic interactions. Mn^{2+} adsorption is self-limited as it stops when all the Ti_2C_3 flake negative charges are counter-balanced. By reacting with MnO_4^- anions at 120 °C, MnO_2 particles gradually and uniformly grow on the flat MXene template. The resulting material morphology can be evidenced by SEM and TEM imaging. From SEM image in Figure 4a, it is difficult to assign any morphology difference between the composite and raw MnO_2 (see Fig. S2c for comparison with MnO_2-120). Moreover, it was not possible to identify anything looking like the pristine Ti_3C_2 MXene flakes in the micrographies. At this stage, we argue this is because they are fully covered by MnO_2 particles. TEM image in Figure 4b is more indicative as it shows a rather homogeneous thick layer of MnO_2 grown at the surface of a microsized Ti_3C_2 MXene flake. The same morphology was found all over the analyzed sample and, either by SEM or TEM, it was not possible to identify any small or individual MnO_2 particles nor individual Ti_3C_2 MXene flake neither uncovered nor partially covered by MnO_2 particles. Consistently, EDX mappings shown in Figure S6 demonstrates the homogeneous distribution of the various components Mn, O, Ti and C, all over the surface of the sample, characteristic of an intimate mixture of MnO_2 and Ti_3C_2 MXene in the composite and confirming the preferential growth of MnO_2 particles at the surface of MXene flakes. Consistently with the self-limited adsorption of Mn^{2+} cations at MXene surface, the same composition was found on every spots analyzed by EDX mapping. EDX analysis (Table S2) also evidenced the presence of K in the composite, as expected intercalated cations in between the layers of δ-MnO_2. As suggested by the SEM images, MnO_2 appears as the predominant component while Ti_3C_2, underneath the MnO_2 thicker layer, is more difficult to accurately detect and analyze.

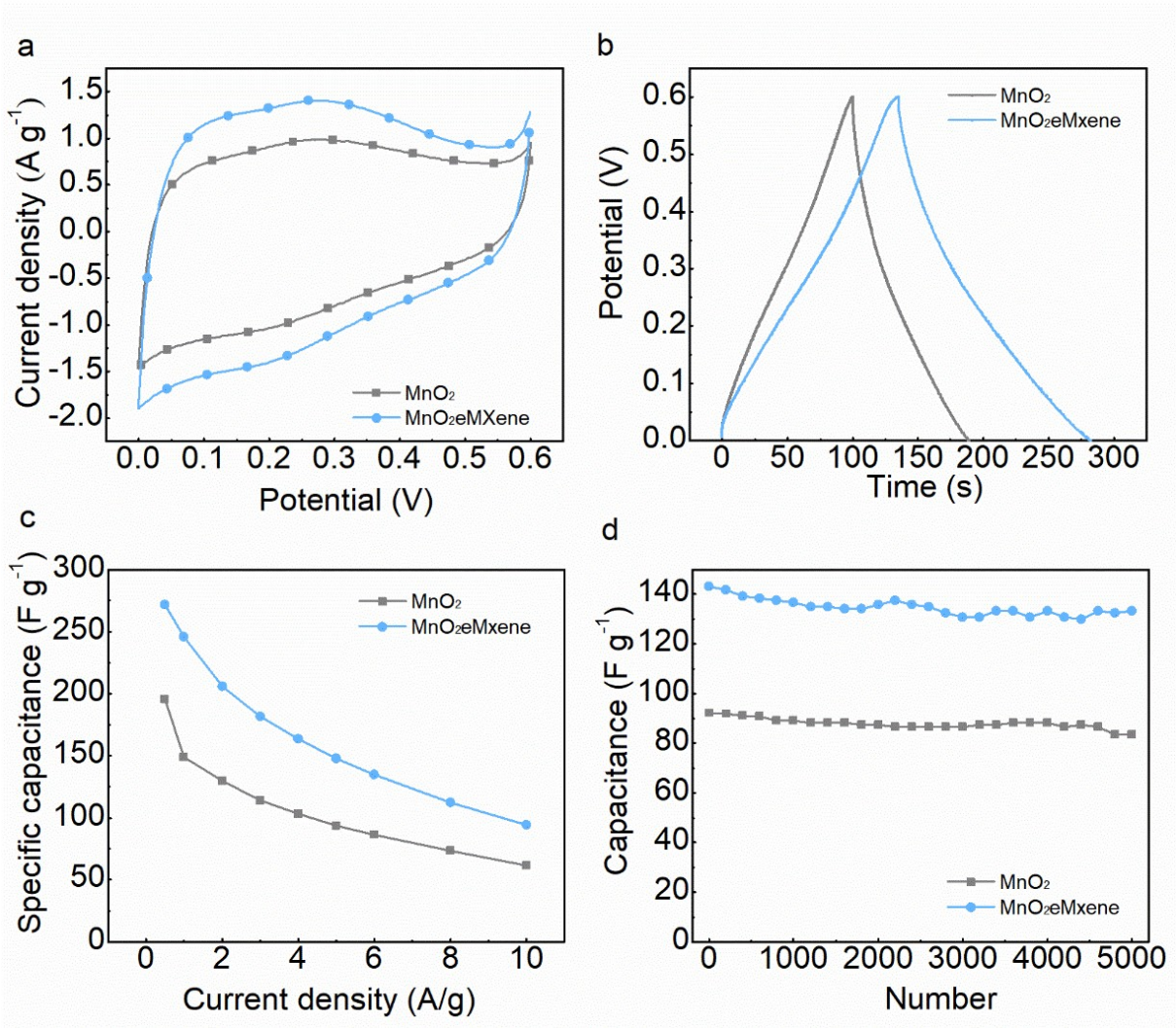

Figure 5. Electrochemical characteristics of MnO_2eMXene composite and MnO_2-120 -based electrodes in 1 M KOH electrolyte. (a) Cyclic voltammetry measurement at 5 mV s^{-1} scan rate. (b) Galvanostatic charge-discharge curves at 1 A g^{-1} current density. (c) Comparison of specific capacitances from galvanostatic measurements at various current densities. (d) Cycling capability over 5k charge-discharge cycles at 5 A g^{-1}.

MnO_2-120 and MnO_2eMXene -based electrodes were used for electrochemical characterization in a three-electrode setup in KOH as well as in Na_2SO_4 electrolytes. In 1M KOH, cyclic voltammograms measured at 5 mV s^{-1} between 0 and 0.6 V versus Hg/HgO reference electrode in Figure 5a are characteristic of a pseudocapacitive electrode material. These CVs, but also the corresponding galvanostatic curves in the same potential range (Fig. 5b), show that the composite displays a greater capacitance than MnO_2-120 electrode. However, both electrode materials have similar rate capabilities (Fig. 5c). As such, the composite can deliver a capacitance of 272 F g^{-1} at 0.5 A g^{-1}, fairly more than MnO_2-120 at 196 F g^{-1} at the same current density, that decreases by 55 % down to 148 F g^{-1} at 5 A g^{-1}. For MnO_2-120 electrode, the capacity loss at 5 A g^{-1} is of 47 % at 94 F g^{-1}. As anticipated, the MnO_2eMXene -based electrode inherits the rate capability of MnO_2-120 demonstrated above. On the other hand, the composite capacitance at 5 A g^{-1} is 133 F g^{-1} after 5k

charge-discharge cycles, corresponding to 93% of its initial capacitance (Fig. 5d). Conversely, the capacitance of MnO_2-120 electrode at 83 F g^{-1} after the same electrochemical cycling program is characteristic of a 90% retention, about the same as using the MnO_2eMXene composite electrode. Electrochemical characteristics of the prepared electrode materials were also tested in sodium sulfate electrolyte. Results are shown in Figure 6. Here again, both MnO_2-120 and MnO_2eMXene -based electrode CVs show roughly rectangular shapes (Fig. 6a) while usual triangular galvanostatic responses are obtained (Fig. 6b). Corresponding capacitances were calculated at various current densities by galvanostatic cycling (but also from CVs at various scan rates in Figure S7 and Table S3). For MnO_2-120 electrode, the capacitance is 114 F g^{-1} at 0.5 A g^{-1} but fades down to 8 F g^{-1} at 10 A g^{-1}, demonstrating the poor rate performance (7%) usually observed for MnO_2-based electrodes in neutral electrolyte.[55,56,62] Oppositely, at higher current, the electrode made of MnO_2eMXene composite can hold almost 50% of its low current capacitance, delivering 165 F g^{-1} (0.5 A g^{-1}) and 81 F g^{-1} (10 A g^{-1}) (Fig. 6c). In neutral electrolyte, the greater rate capabilities of MnO_2eMXene can hardly be assigned to some α-MnO_2 contribution as in KOH electrolyte for two reasons. Firstly, the rate capability of α-MnO_2 has been shown to be very limited in Na_2SO_4 1M.[62] Secondly, despite the same synthesis temperature, there is not much evidence of any needle in the SEM/TEM micrographies of MnO_2eMXene composite or α-MnO_2 diffraction peaks in its XRD pattern. The enhanced rate performance of MnO_2eMXene should be assigned to the enhanced electronic conductivity thanks to the MXene component. The cycling capability over 5k cycles was evaluated at 5 A g^{-1} current density (Fig.6d). For both prepared electrode materials, there is not any noticeable capacitance fading, demonstrating the good stability of these pseudocapacitive materials upon cycling at this quite realistic regime (from 40 to 60 sec. for a complete charge discharge cycle). At this stage, the contribution of the MXene core to the cycling capability of composite electrodes could not be assessed as, either in KOH or Na_2SO_4 electrolytes, capacitance retention of MnO_2 and MnO_2eMXene -based electrodes remained close to 100 % after 5k charge-discharge cycles.

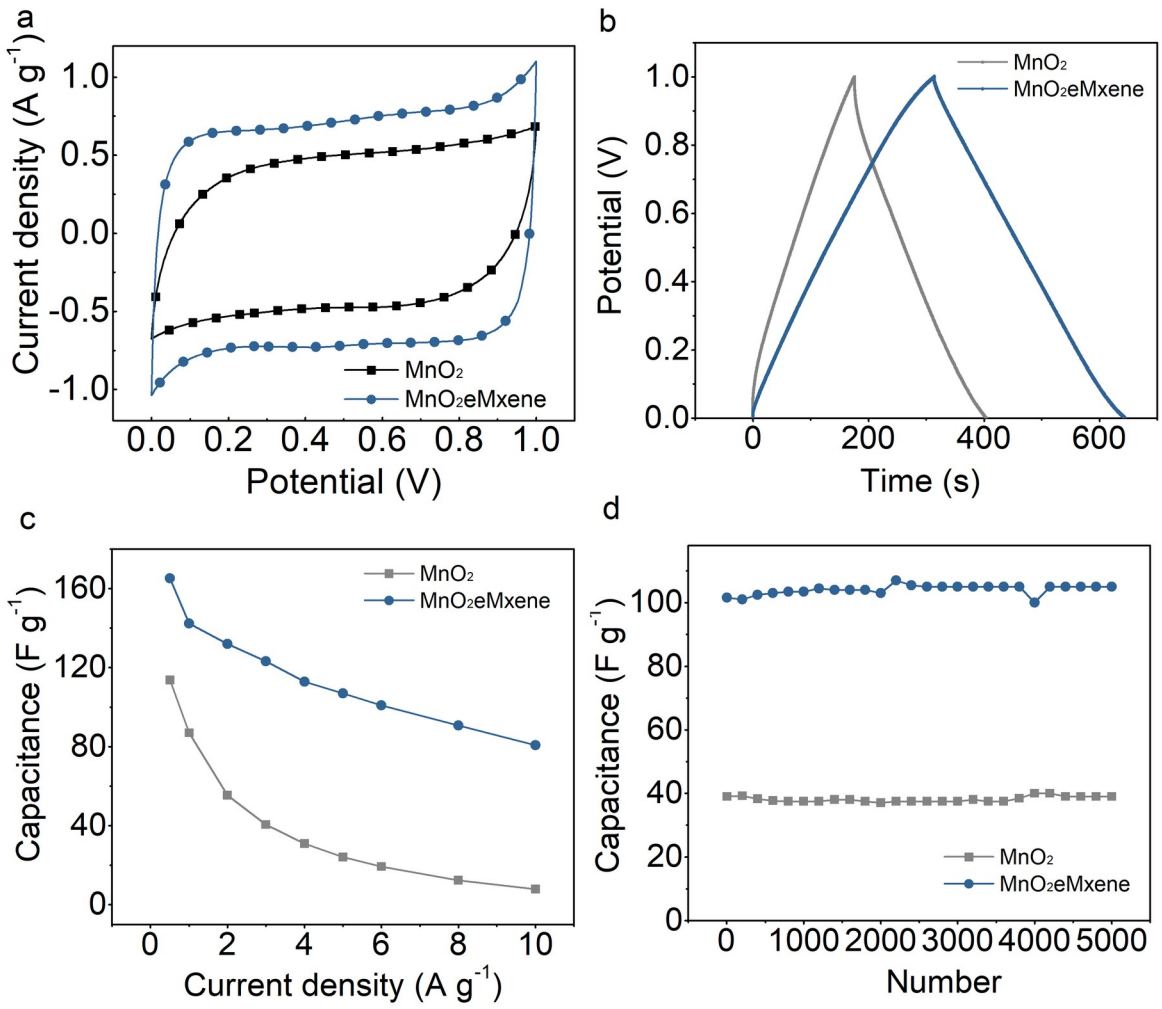

Figure 6. Electrochemical characteristics of of MnO_2eMXene composite and MnO_2-120 -based electrodes in 1 M Na_2SO_4 electrolyte. (a) CV curves at 5 mV s^{-1} scan rate. (b) Galvanostatic charge discharge curves at 0.5 A g^{-1} current density. (c) Comparison of specific capacitances from galvanostatic measurements at various current densities. (d) Cyclic stability after 5k charge-discharge cycles at 5 A g^{-1}.

Two-electrode asymmetric devices were assembled from an activated carbon (AC) used as negative electrode and MnO_2eMXene composite (MeM) as positive electrode. Mass loadings were balanced based on capacitance values calculated from galvanostatic charge-discharge measurements at the same current density in corresponding electrolytes. They were tested in KOH as well as Na_2SO_4 electrolytes. From CV as well as from galvanostatic measurements (Figs. 7a and 7b), the AC//MeM device was operated in a greater voltage window of 2.0 V in Na_2SO_4 electrolyte (AC//MeM-Na)[54] while it was limited to 1.6 V in KOH (AC//MeM-K). In contrast, the capacitance of the device (relative to the mass of both electrodes) is lower in Na_2SO_4 electrolyte (35 F g^{-1}) than in KOH (47 F g^{-1}) and the difference is obviously assigned to the greater capacitance of the MnO_2eMXene positive electrode in the latter electrolyte (Fig. 5a and 6a: 272 F g^{-1} in KOH versus 165 F g^{-1} than in Na_2SO_4). This balance of both device capacitance and voltage leads to energy densities in the same range (Fig. 7c). These were calculated from galvanostatic

charge-discharge data. The AC//MeM-Na device shows an energy density of 19.3 Wh kg^{-1} at 500 W kg^{-1}, while the value decreased to 4.4 Wh kg^{-1} at 10k W kg^{-1}. AC//MeM-K device presents 11 Wh kg^{-1} energy density at 8k W kg^{-1}, although it showed 16.8 Wh kg^{-1} at 400 W kg^{-1}, revealing an attractive energy-density retention at high power. The cycling stability was also evaluated for both devices (Fig. 7d). After 10k charge-discharge cycles, capacitances of both devices operated in KOH and Na_2SO_4 electrolytes decreased to about 77% of their initial capacitance. Most of the loses occurred during the first 2k cycles. To assign the origin of these fadings, Ohmic drop as well as Coulombic and energy efficiencies were analyzed (Fig. S3). In KOH electrolyte, the apparent decrease of specific capacitance during the first 2000 cycles can be assigned to the observed evident reduction of the energy efficiency. Then, the device suffered a gradual capacitive decay in extra cycles. On the other hand, there are also a visible fading of the energy efficiency over initial 1000 cycles when the device was operated in Na_2SO_4 electrolyte, though the capacitance fading is more limited. Additionally, it exhibits slight increase of Ohmic drop over cycles in both applied electrolytes.

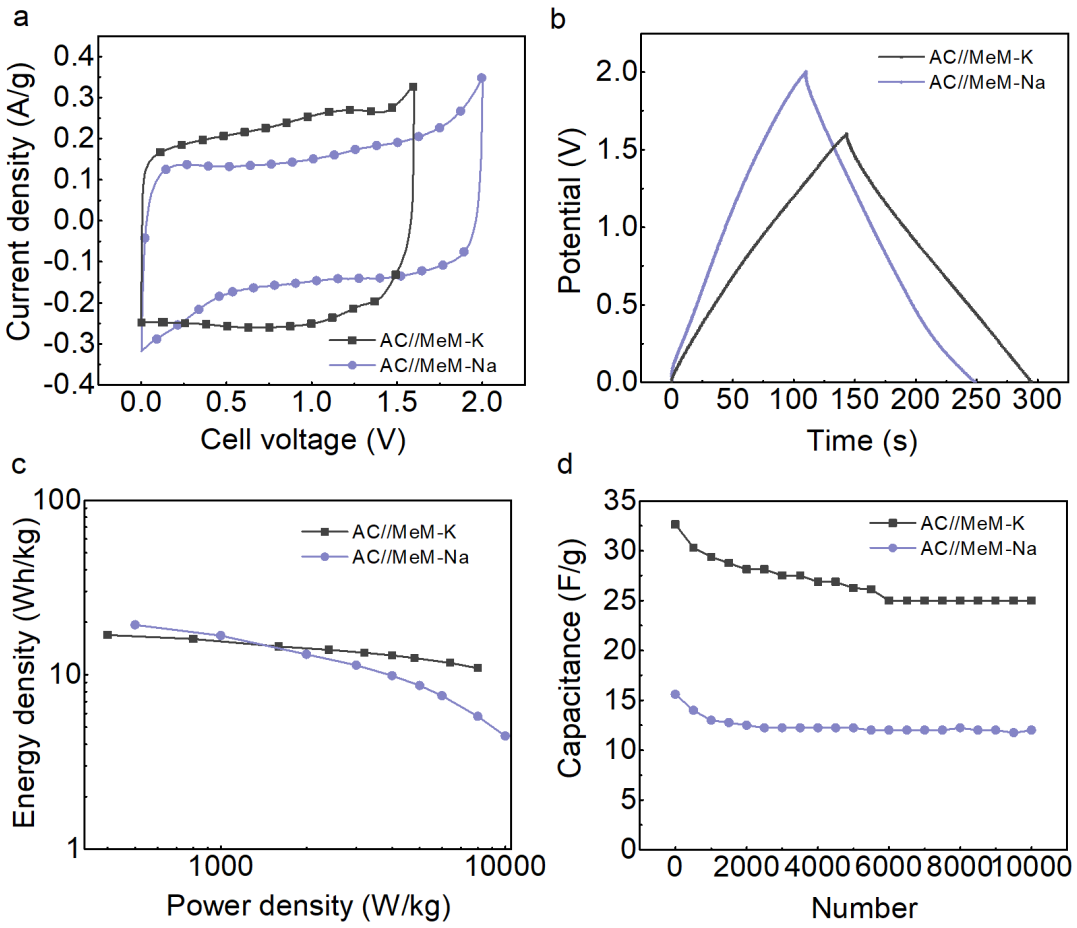

Figure 7. The electrochemical performance of AC//MeM-K and AC//MeM-Na devices in neutral (Na_2SO_4 1 M) and alkaline electrolytes (KOH 1 M). (a) Cyclic voltammetry test at 20 mV s^{-1}. (b) galvanostatic charge discharge curve at 0,5 A g^{-1}. (b) Ragone plots for the full cell. Power and energy densities are normalized by the mass of both electrodes. (d) Cycling Longevity in 10k charge-discharge cycles.

CONCLUSION

Two different MnO_2 polymorphs and their mixtures were synthesized by adjusting the temperature of the co-precipitation reaction. According to XRD patterns and SEM images, below 80 °C, δ-MnO_2 was obtained while α-MnO_2 was prepared at greater temperatures. This structural change was evidenced as the powder morphology evolved from δ-MnO_2 nano-sheets to α-MnO_2 nano-fibers. Moreover, MnO_2-120 sample prepared at 120 °C appeared as a mixture of δ and α phases with nano-sheets and fibers. As an electrode in a three-electrode setup, MnO_2-120 electrode not only exhibited a high capacitance (196 F g^{-1} at 0.5 A g^{-1}) just like δ-MnO_2, but also held the rate performance of α-MnO_2. Exfoliated Ti_3C_2 MXene layers with negative surface charges were introduced in the co-precipitation medium, allowing Mn^{2+} cations to adsorb while reacting at 120 °C with Mn^{7+} to give MnO_2 sand-roses particles grown at the MXene layer surface. The resulting composite was characterized by X-ray powder diffraction and electron microscope measurements. An MnO_2eMXene -based electrode was initialy studied in a three-electrode cell, using KOH and Na_2SO_4 electrolytes. In KOH it delivered a capacitance performance of 272 F g^{-1} at 0.5 A g^{-1} and kept 93% of capacitance retention over 5k charge-discharge cycles at a current density as high as 5 A g^{-1}. On the other hand, in Na_2SO_4 electrolyte, MnO_2eMXene electrode showed a 165 F g^{-1} capacitance at 0.5 A $g^{-1}$and 81 F g^{-1} at 10 A g^{-1}, implying a 50% of rate capability in this current range. From 106 F g^{-1}, any capacitance fading could be observed over 5k charge-discharge cycles at 5 A g^{-1} current density. In a second step, asymmetric devices built on MnO_2eMXene (MeM) and commercial activated carbon in both electrolytes were fabricated and evaluated. Compared with the AC//MeM-K operated in KOH owning a 1.6 V working voltage window, AC//MeM-Na device takes benefit from a larger potential window of 2 V in Na2SO4, confirming the advantages of neutral electrolytes. As such, AC//MeM-Na displayed a 19.3 Wh kg^{-1} (500 W kg^{-1} power density) energy density while it was 16.8 Wh kg^{-1} at 400 W kg^{-1} for AC//MeM-K. In contrast, AC//MeM-Na showed a drastic energy-density fading at 4.4 Wh kg^{-1} at 10 KW kg^{-1}, while AC//MeM-K device kept a remarkable energy density of 11 Wh kg^{-1} at a 8 KW kg^{-1} power density.

ACKNOWLEDGMENT

Y.C. Zhu PhD fellowship (NO. 201606240097) is supported by China Scholarship Council (CSC).
F. Favier and P. Simon thank the Agence Nationale de la Recherche (ANR, Labex STOREX) for support.

REFERENCES

1. Y. Gogotsi, P. Simon, Materials for electrochemical capacitors, Nat. Mater. 7 (2008) 845–854.
2. F. Béguin, V. Presser, A. Balducci, E. Frackowiak, Carbons and electrolytes for advanced supercapacitors, Adv. Mater. 26 (2014) 2219–2251.

3. P. Simon, Y. Gogotsi, B. Dunn, Where Do Batteries End and Supercapacitors Begin?, Science 343 (6176) (2014) 1210–1211.
4. W. Bao, L. Liu, C. Wang, S. Choi, D. Wang, G. Wang, Facile Synthesis of Crumpled Nitrogen-Doped MXene Nanosheets as a New Sulfur Host for Lithium–Sulfur Batteries, Adv. Energy Mater. 8 (2018) 1–11.
5. M. Salanne, B. Rotenberg, K. Naoi, K. Kaneko, P.-L. Taberna, C.P. Grey, B. Dunn, P. Simon, Efficient storage mechanisms for building better supercapacitors, Nat. Energy 1 (2016) 16070.
6. F. Wang, X. Wu, X. Yuan, Z. Liu, Y. Zhang, L. Fu, Y. Zhu, Q. Zhou, Y. Wu, W. Huang, Latest advances in supercapacitors: From new electrode materials to novel device designs, Chem. Soc. Rev. 46 (2017) 6816–6854.
7. X. Chen, R. Paul, L. Dai, Carbon-based supercapacitors for efficient energy storage, Natl. Sci. Rev. 4 (2017) 453–489.
8. S. Bose, T. Kuila, A.K. Mishra, R. Rajasekar, N.H. Kim, J.H. Lee, Carbon-based nanostructured materials and their composites as supercapacitor electrodes, J. Mater. Chem. 22 (2012) 767–784.
9. C. Merlet, B. Rotenberg, P.A. Madden, P.L. Taberna, P. Simon, Y. Gogotsi, M. Salanne, On the molecular origin of supercapacitance in nanoporous carbon electrodes, Nat. Mater. 11 (2012) 306–310.
10. J. Wang, J. Tang, B. Ding, V. Malgras, Z. Chang, X. Hao, Y. Wang, H. Dou, X. Zhang, Y. Yamauchi, Hierarchical porous carbons with layer-by-layer motif architectures from confined soft-template self-assembly in layered materials, Nat. Commun. 8 (2017) 1–9.
11. G. Li, J. Sun, W. Hou, S. Jiang, Y. Huang, J. Geng, Three-dimensional porous carbon composites containing high sulfur nanoparticle content for high-performance lithium-sulfur batteries, Nat. Commun. 7 (2016) 1–10.
12. M. Yang, Z. Zhou, Recent Breakthroughs in Supercapacitors Boosted by Nitrogen-Rich Porous Carbon Materials, Adv. Sci. 4 (2017) 1600408.
13. A.M. Abioye, F.N. Ani, Recent development in the production of activated carbon electrodes from agricultural waste biomass for supercapacitors: A review, Renew. Sustain. Energy Rev. 52 (2015) 1282–1293.
14. A. Borenstein, O. Hanna, R. Attias, S. Luski, T. Brousse, D. Aurbach, Carbon-based composite materials for supercapacitor electrodes: A review, J. Mater. Chem. A 5 (2017) 12653–12672.
15. W. Hooch Antink, Y. Choi, K.D. Seong, J.M. Kim, Y. Piao, Recent Progress in Porous Graphene and Reduced Graphene Oxide-Based Nanomaterials for Electrochemical Energy Storage Devices, Adv. Mater. Interfaces 5 (2018) 1–19.
16. R. Raccichini, A. Varzi, S. Passerini, B. Scrosati, The role of graphene for electrochemical energy storage, Nat. Mater. 14 (2015) 271–279.
17. M.F. El-Kady, S. Veronica, D. Sergey, B.K. Richard, Laser Scribing of High-Performance and Flexible Graphene-Based Electrochemical Capacitors, Science 335 (2012) 1326–1330.

18. A. Eftekhari, The mechanism of ultrafast supercapacitors, J. Mater. Chem. A 6 (2018) 2866–2876.
19. D.P. Dubal, O. Ayyad, V. Ruiz, P. Gómez-Romero, Hybrid energy storage: The merging of battery and supercapacitor chemistries, Chem. Soc. Rev. 44 (2015) 1777–1790.
20. M. Zhi, C. Xiang, J. Li, M. Li, N. Wu, Nanostructured carbon-metal oxide composite electrodes for supercapacitors: A review, Nanoscale 5 (2013) 72–88.
21. C. (John) Zhang, T.M. Higgins, S.H. Park, S.E. O'Brien, D. Long, J.N. Coleman, V. Nicolosi, Highly flexible and transparent solid-state supercapacitors based on RuO2/PEDOT:PSS conductive ultrathin films, Nano Energy 28 (2016) 495–505.
22. H. Li, X. Li, J. Liang, Y. Chen, Hydrous RuO2 Decorated MXene Coordinating with Silver Nanowire Inks Enabling Fully Printed Micro-Supercapacitors with Extraordinary Volumetric Performance, Adv. Energy Mater. 9 (2019), 1803987.
23. H. Ma, D. Kong, Y. Xu, X. Xie, Y. Tao, Z. Xiao, W. Lv, H.D. Jang, J. Huang, Q.H. Yang, Disassembly–Reassembly Approach to RuO2/Graphene Composites for Ultrahigh Volumetric Capacitance Supercapacitor, Small 13 (2017) 1–7.
24. Y. Wang, D. Gu, J. Guo, M. Xu, H. Sun, J. Li, L. Wang, L. Shen, Maximized Energy Density of RuO2//RuO2 Supercapacitors through Potential Dependence of Specific Capacitance, ChemElectroChem 7 (2020) 928–936.
25. T. Liu, Z. Zhou, Y. Guo, D. Guo, G. Liu, Block copolymer derived uniform mesopores enable ultrafast electron and ion transport at high mass loadings, Nat. Commun. 10 (2019) 1–10.
26. N. Zhang, F. Cheng, J. Liu, L. Wang, X. Long, X. Liu, F. Li, J. Chen, Rechargeable aqueous zinc-manganese dioxide batteries with high energy and power densities, Nat. Commun. 8 (2017) 1–9.
27. H. Chen, L. Hu, Y. Yan, R. Che, M. Chen, L. Wu, One-step fabrication of ultrathin porous nickel hydroxide-manganese dioxide hybrid nanosheets for supercapacitor electrodes with excellent capacitive performance, Adv. Energy Mater. 3 (2013) 1636–1646.
28. M.R. Lukatskaya, B. Dunn, Y. Gogotsi, Multidimensional materials and device architectures for future hybrid energy storage, Nat. Commun. 7 (2016) 1–13.
29. S. Yoon, E. Kang, J.K. Kim, C.W. Lee, J. Lee, Development of high-performance supercapacitor electrodes using novel ordered mesoporous tungsten oxide materials with high electrical conductivity, Chem. Commun. 47 (2011) 1021–1023.
30. D.P. Dubal, S.H. Lee, J.G. Kim, W.B. Kim, C.D. Lokhande, Porous polypyrrole clusters prepared by electropolymerization for a high performance supercapacitor, J. Mater. Chem. 22 (2012) 3044–3052.
31. G. Yu, L. Hu, N. Liu, H. Wang, M. Vosgueritchian, Y. Yang, Y. Cui, Z. Bao, Enhancing the supercapacitor performance of graphene/MnO2 nanostructured electrodes by conductive wrapping, Nano Lett. 11 (2011) 4438–4442.

32. M. Kim, C. Lee, J. Jang, Fabrication of highly flexible, scalable, and high-performance supercapacitors using polyaniline/reduced graphene oxide film with enhanced electrical conductivity and crystallinity, Adv. Funct. Mater. 24 (2014) 2489–2499.
33. Z. Ma, G. Shao, Y. Fan, G. Wang, J. Song, D. Shen, Construction of Hierarchical α-MnO2 Nanowires@Ultrathin δ-MnO2 Nanosheets Core-Shell Nanostructure with Excellent Cycling Stability for High-Power Asymmetric Supercapacitor Electrodes, ACS Appl. Mater. Interfaces 8 (2016) 9050–9058.
34. X. Zhao, L. Zhang, S. Murali, M.D. Stoller, Q. Zhang, Y. Zhu, R.S. Ruoff, Incorporation of manganese dioxide within ultraporous activated graphene for high-performance electrochemical capacitors, ACS Nano 6 (2012) 5404–5412.
35. D.Y. Sung, I.Y. Kim, T.W. Kim, M.S. Song, S.J. Hwang, Room temperature synthesis routes to the 2D nanoplates and 1D nanowires/nanorods of manganese oxides with highly stable pseudocapacitance behaviors, J. Phys. Chem. C 115 (2011) 13171–13179.
36. Z. Lv, Y. Luo, Y. Tang, J. Wei, Z. Zhu, X. Zhou, W. Li, Y. Zeng, W. Zhang, Y. Zhang, D. Qi, S. Pan, X.J. Loh, X. Chen, Editable Supercapacitors with Customizable Stretchability Based on Mechanically Strengthened Ultralong MnO2 Nanowire Composite, Adv. Mater. 30 (2018) 1704531.
37. A. Cross, A. Morel, A. Cormie, T. Hollenkamp, S. Donne, Enhanced manganese dioxide supercapacitor electrodes produced by electrodeposition, J. Power Sources 196 (2011) 7847–7853.
38. C. Choi, K.M. Kim, K.J. Kim, X. Lepró, G.M. Spinks, R.H. Baughman, S.J. Kim, Improvement of system capacitance via weavable superelastic biscrolled yarn supercapacitors, Nat. Commun. 7 (2016) 1–8.
39. M. Ghidiu, M.R. Lukatskaya, M.Q. Zhao, Y. Gogotsi, M.W. Barsoum, Conductive two-dimensional titaniumcarbide ‘clay’ with high volumetric capacitance, Nature 516 (2015) 78–81.
40. F. Shahzad, M. Alhabeb, C.B. Hatter, B. Anasori, S.M. Hong, C.M. Koo, Y. Gogotsi, Electromagnetic interference shielding with 2D transition metal carbides (MXenes), Science 353 (2016) 1137–1140.
41. M. Khazaei, M. Arai, T. Sasaki, C.Y. Chung, N.S. Venkataramanan, M. Estili, Y. Sakka, Y. Kawazoe, Novel electronic and magnetic properties of two-dimensional transition metal carbides and nitrides, Adv. Funct. Mater. 23 (2013) 2185–2192.
42. X. Liang, A. Garsuch, L.F. Nazar, Sulfur Cathodes Based on ConductiveMXene Nanosheets for High- Performance Lithium–Sulfur Batteries, Angew. Chemie-Int. Ed. 54 (2015) 3907–3911.
43. L. Ding, Y. Wei, Y. Wang, H. Chen, J. Caro, H. Wang, A Two-Dimensional Lamellar Membrane:MXene NanosheetStacks, Angew. Chemie - Int. Ed. 56 (2017) 1825–1829.
44. M.R. Lukatskaya, S. Kota, Z. Lin, M.Q. Zhao, N. Shpigel, M.D. Levi, J. Halim, P.L. Taberna, M.W. Barsoum, P. Simon, Y. Gogotsi, Ultra-high-rate pseudocapacitive energy storage in two-dimensional transition metal carbides, Nat. Energy. 6 (2017) 1–6.

45. C. Couly, M. Alhabeb, K.L. Van Aken, N. Kurra, L. Gomes, A.M. Navarro-Suárez, B. Anasori, H.N. Alshareef, Y. Gogotsi, Asymmetric Flexible MXene-Reduced Graphene Oxide Micro-Supercapacitor, Adv. Electron. Mater. 4 (2018) 1–8.
46. Q. Xue, Z. Pei, Y. Huang, M. Zhu, Z. Tang, H. Li, Y. Huang, N. Li, H. Zhang, C. Zhi, Mn3O4 nanoparticles on layer-structured Ti3C2 MXene towards the oxygen reduction reaction and zinc-air batteries, J. Mater. Chem. A. 5 (2017) 20818–20823.
47. C. Chen, X. Xie, B. Anasori, A. Sarycheva, T. Makaryan, M. Zhao, P. Urbankowski, L. Miao, J. Jiang, Y. Gogotsi, MoS2-on-MXene Heterostructures as Highly Reversible Anode Materials for Lithium-Ion Batteries, Angew. Chemie - Int. Ed. 57 (2018) 1846–1850.
48. S. Niu, Z. Wang, M. Yu, M. Yu, L. Xiu, S. Wang, X. Wu, J. Qiu, MXene-Based Electrode with Enhanced Pseudocapacitance and Volumetric Capacity for Power-Type and Ultra-Long Life Lithium Storage, ACS Nano 12 (2018) 3928–3937.
49. L. Yu, L. Hu, B. Anasori, Y.T. Liu, Q. Zhu, P. Zhang, Y. Gogotsi, B. Xu, MXene-Bonded Activated Carbon as a Flexible Electrode for High-Performance Supercapacitors, ACS Energy Lett. 3 (2018) 1597–1603.
50. C. Yang, Y. Tang, Y. Tian, Y. Luo, Y. He, X. Yin, W. Que, Achieving of Flexible, Free-Standing, Ultracompact Delaminated Titanium Carbide Films for High Volumetric Performance and Heat-Resistant Symmetric Supercapacitors, Adv. Funct. Mater. 28 (2018) 1705487.
51. R.B. Rakhi, B. Ahmed, D. Anjum, H.N. Alshareef, Direct Chemical Synthesis of MnO2 Nanowhiskers on Transition-Metal Carbide Surfaces for Supercapacitor Applications, ACS Appl. Mater. Interfaces 8 (2016) 18806–18814.
52. O. Ghodbane, J.L. Pascal, F. Favier, Microstructural effects on charge-storage properties in MnO 2-based electrochemical supercapacitors, ACS Appl. Mater. Interfaces 1 (2009) 1130–1139.
53. L. Athouël, F. Moser, R. Dugas, O. Crosnier, D. Bélanger, T. Brousse, Variation of the MnO2 birnessite structure upon charge/discharge in an electrochemical supercapacitor electrode in aqueous Na2SO4 electrolyte, J. Phys. Chem. C 112 (2008) 7270–7277.
54. T. Brousse, P.-L. Taberna, O. Crosnier, R. Dugas, P. Guillemet, Y. Scudeller, Y. Zhou, F. Favier, D. Bélanger, P. Simon, Long-term cycling behavior of asymmetric activated carbon/MnO2 aqueous electrochemical supercapacitor, J. Power Sources 173 (2007) 633–641.
55. M. Toupin, T. Brousse, D. Bélanger, Charge storage mechanism of MnO2 electrode used in aqueous electrochemical capacitor, Chem. Mater. 16 (2004) 3184–3190.
56. A. Gambou-Bosca, D. Bélanger, Electrochemical characterization of MnO2-based composite in the presence of salt-in-water and water-in-salt electrolytes as electrode for electrochemical capacitors, J. Power Sources 326 (2016) 595–603.
57. A.A. Voskanyan, C.-K. Ho, K.Y. Chan, 3D δ-MnO2 nanostructure with ultralarge mesopores as high-performance lithium-ion battery anode fabricated via colloidal solution combustion synthesis, J. Power Sources 421 (2019) 162–168.

58. Cong Guo, Qihao Zhou, Huimin Liu, Shuo Tian, Binglei Chen, Jian Zhao, Jingfa Li, A case study of β- and δ-MnO_2 with different crystallographic forms on ion-storage in rechargeable aqueous zinc ion battery, Electrochimica Acta 324 (2019) 134867.
59. J. Yan, C.E. Ren, K. Maleski, C.B. Hatter, B. Anasori, P. Urbankowski, A. Sarycheva, Y. Gogotsi, Flexible MXene/Graphene Films for Ultrafast Supercapacitors with Outstanding Volumetric Capacitance, Adv. Funct. Mater. 27 (2017) 1–10.
60. K. Huang, Z. Li, J. Lin, G. Han, P. Huang, Two-dimensional transition metal carbides and nitrides (MXenes) for biomedical applications, Chem. Soc. Rev. 47 (2018) 5109–5124.
61. L. Ding, Y. Wei, Y. Wang, H. Chen, J. Caro, H. Wang, A Two-Dimensional Lamellar Membrane: MXene Nanosheet Stacks, Angew. Chemie - Int. Ed. 56 (2017) 1825–1829.
62. H.U. Shah, F. Wang, M.S. Javed, R. Saleem, M.S. Nazir, J. Zhan, Z.U.H. Khan, M.U. Farooq, S. Ali, Synthesis, characterization and electrochemical properties of α-MnO2 nanowires as electrode material for supercapacitors, Int. J. Electrochem. Sci. 13 (2018) 6426–6435.